Journal of the Mechanical Behavior of Biomedical Materials 183 (2026) 107607

Contents lists available at ScienceDirect

Journal of the Mechanical Behavior of Biomedical Materials

journal homepage: www.elsevier.com/locate/jmbbm

Toward accurate regional lung strain quantification from microCT data: insights and limitations of digital volume correlation

Kaveh Ahookhosh [a,b], Grzegorz Pyka [b], Lara Mazy [b,c,d], Greet Kerckhofs [b,c,d,e,1], Greetje Vande Velde [a,*,1]

[a] Biomedical MRI, Department of Imaging and Pathology, KU Leuven, Belgium
[b] Institute of Mechanics, Materials, and Civil Engineering (iMMC), UCLouvain, Belgium
[c] Deparment of Materials Engineering, KU Leuven, Belgium
[d] Institute of Experimental and Clinical Research (IREC), UCLouvain, Belgium
[e] Prometheus, Division for Skeletal Tissue Engineering, KU Leuven, Belgium

A B S T R A C T

The biomechanics of the lung plays a crucial role in respiratory function, and its alteration is closely linked to the onset and progression of lung diseases. Quantifying local strain within lung tissue is essential for understanding how lung mechanics influence pulmonary function and disease progression. Digital Volume Correlation (DVC) provides a non-destructive method to quantify 3D strain fields in biological tissues, but its accuracy depends on multiple parameters, which remain poorly characterized in soft tissues. In this study, we evaluated the accuracy of DVC, using both local and global approaches, for lung tissue imaged with high-resolution contrast-enhanced computed tomography (HR CECT) and assessed its potential application throughout a range of lower resolution and noisier data towards HR *ex vivo* and *in vivo* microCT data. We investigated the effects of DVC settings, lung microstructure, and input image quality, including noise level and voxel size. Synthetic deformations of known magnitudes (1-5%) were applied to optimize subvolume and mesh sizes, with mean metric values and correlation residuals used to evaluate registration quality. Strain measurements from global DVC were highly sensitive to mesh size, with optimal meshes yielding robust estimates, while larger meshes reduced accuracy. Correlation residuals reliably identified the optimal mesh size as a global registration metric. Adding Gaussian noise demonstrated that higher noise levels reduced DVC accuracy, particularly at larger deformations and with non-optimal meshes. Downscaling imaging data increased voxel size in a range from 3.8 μm to 30.4 μm left central strain distributions largely unchanged, but induced boundary-related errors with regions of high strain intensity near sample boundaries highlighting the need for sufficiently large volumes of interest at large voxel sizes for DVC-based strain analysis. Within these limitations, DVC effectively captured regional lung strain, supporting its applicability from HR CECT data to *ex vivo* HR microCT. Our findings provide critical insights into how DVC operational parameters, across both local and global approaches, tissue microarchitecture and input imaging quality affect the accuracy of strain measurements in soft tissues. By demonstrating the feasibility of DVC for lung strain analysis using microCT data, this study provides a foundation for further research into the use of strain measurements to characterize lung biomechanics in animal models at study endpoints with *ex vivo* HR microCT.

1. Introduction

Lung diseases are a serious global public health issue and rank among the leading causes of death worldwide (Soriano et al., 2020). They can stem from various sources such as environmental pollutants and toxins, social habits like smoking or vaping, or lung infections, fibrosis or cancer. Understanding the impact of these lung diseases on lung microstructure and mechanics is crucial for linking structural alterations to lung dysfunction and for discovering novel biomarkers that facilitate early diagnosis and longitudinal assessment of disease progression. This knowledge enables discovery of new treatments, as well as determining the optimal timing and methods for their application. Gaining this knowledge from lung disease models requires sensitive, regional diagnostic and monitoring tools, ideally acquired in a non-invasive and non-destructive way. Most of the current methods for lung assessments in animal models, including lung function tests, consider the lungs as a single unit and deliver global readouts. Imaging-based methods remain underexploited despite their potential to provide insights into the regional impact of diseases on lung anatomy and physiology, thereby helping to bridge gaps in current knowledge (Pennati et al., 2023; Broche et al., 2017; Cercos-Pita et al., 2022; Deyhle et al., 2025). Among conventional lung imaging modalities, such as micro-focus X-ray computed tomography (microCT), magnetic resonance imaging (MRI) and nuclear imaging techniques (PET/SPECT), microCT is a preferred

* Corresponding author.
E-mail address: greetje.vandevelde@kuleuven.be (G. Vande Velde).
[1] These authors share last authorship.

https://doi.org/10.1016/j.jmbbm.2026.107607
Received 21 April 2026; Received in revised form 19 August 2026; Accepted 28 August 2026
Available online 5 September 2026

choice for experimental lung imaging due to its high spatial resolution and relatively fast and straightforward imaging protocols. In addition to high-resolution (HR) 3D visualization of both the interior and exterior of samples, microCT enables respiratory-gated acquisitions synchronized with the breathing cycle, allowing motion-reduced imaging and phase-specific assessment of lung structure and volumetric changes between phases. In biomedical research, lung microCT has found various applications such as diagnosis of lung pathologies (Langhe et al., 2012; Vande et al., 2016; Dekoster et al., 2020; Tielemans et al., 2020; Ahookhosh et al., 2021; Maes et al., 2022), and longitudinal studies for treatment effects (Dekoster et al., 2020; Schaad et al., 2017; Steiner et al., 2020; Karagiannidis et al., 2021).

On one hand, *in vivo* microCT enables longitudinal functional and structural evaluation of lung disease progression in small-animal models (Langhe et al., 2012; Vande et al., 2016; Dekoster et al., 2020; Ahookhosh et al., 2023, 2025), without significant biological effects from repeated exposure to ionizing radiation with typical voxel sizes around 50 μm (Berghen et al., 2019; Dekoster et al., 2020). HR *in vivo* microCT with smaller voxels is still possible where ionizing radiation is less of a concern or fewer repeat scans are needed (Vande et al., 2015; Vasilescu et al., 2012). On the other hand, *ex vivo* microCT of isolated lung samples provides HR images that allow precise quantitative assessment of lung microstructure at voxel sizes around 10 μm (Albers et al., 2018; Katsamenis et al., 2019; Eckermann et al., 2020; Reiser et al., 2024). While mineralized tissues strongly attenuate X-rays, the constituents of unmineralized soft tissues, including lung tissue, exhibit weaker attenuation in contrast to air or surrounding soft tissues and media. Therefore, contrast-enhancing techniques such as phase-contrast microCT and contrast-enhanced microCT (CECT) can be applied to enhance the visualization of soft tissue components (Mazy and Kerckhofs, 2025). Recent advances in microCT field have enabled image registration techniques as powerful tools for studying 3D displacement and strain fields in both hard-biological tissues, such as bones (Liu and Morgan, 2007a; Palanca et al., 2017a; Comini et al., 2019a), and soft-biological tissues, such as lungs (Arora et al., 2017, 2021, 2024). Since lung abnormalities are linked to elevated and heterogeneous distribution of tissue biomechanical strains (Paula et al., 2016; Herrmann et al., 2018), strain maps of lung provide valuable regional insights into pulmonary behavior and function (Arora et al., 2021; Gattinoni et al., 2012; Maghsoudi-Ganjeh et al., 2021). Multiple attempts have been made to produce strain maps of lung during the respiration using techniques such as digital image correlation (DIC), a novel method for analyzing surface deformations (Maghsoudi-Ganjeh et al., 2021; Mariano et al., 2020, 2022; Nelson et al., 2023). DIC computation is based on sequential images of a speckled sample surface as it undergoes loading, thereby producing a topological displacement field (Chu et al., 1985). Combining a DIC setup with a pressure-volume ventilator to simulate the respiratory process has been successfully employed to quantify surface deformation and strain fields, enabling the investigation of lung biomechanics (Mariano et al., 2022; Nelson et al., 2023; Sattari et al., 2020). In a study using the same experimental setup, pressure-volume and pressure-strain curves were measured from both fibrotic and healthy mouse lungs to investigate ventilator-induced lung injury in healthy and diseased mice (Nelson et al., 2023). Comparing local and global lung compliance and strain patterns between healthy and fibrotic mice revealed a higher susceptibility to ventilator-induced lung injury in fibrotic mice. The main limitation of DIC computation is its reliance on the specimen's speckled surface to measure the displacement field, and the fact that it does not provide any information about internal tissue deformation and strain. Furthermore, creating the speckle pattern on the lung surface before DIC computation requires removing the lung from the animal's body, resulting in unnatural positioning during strain measurement.

DVC, an extension of the DIC technique (Pan, 2018), is capable of producing 3D volumetric displacement and strain maps of biological structures, based on the volumetric images of the reference and deformed states of the specimen during a deformation process due to a biomechanical load. In contrast to DIC, DVC enables the measurement of 3D displacement and strain fields within the complex internal structures of biological specimens (Pan, 2018). The application of DVC analysis is well-established in the field of biomechanics for studying hard biological tissues (Palanca et al., 2016; Buljac et al., 2018; Garavelli et al., 2025; Didziokas et al., 2024). However, despite its great potential, soft tissues such as the lung remain relatively underexplored using DVC compared with other biomaterials (Arora et al., 2021). In recent years, a few studies have utilized synchrotron radiation microCT with an 8 μm imaging voxel size and a limited field of view, combined with DVC, to enhance the understanding of lung mechanics in trauma by analyzing the microstructural deformation of lung tissues (Arora et al., 2017, 2021, 2024). DVC-generated 3D strain maps have been used to distinguish healthy from blast-injured lung tissue by revealing differences in alveolar deformation (Arora et al., 2017). Subsequent studies correlated regional lung strains with ventilation during mechanical ventilation and demonstrated the ability of strain maps to identify areas of poor ventilation (Arora et al., 2021). More recently, synchrotron radiation microCT (8 μm voxel size) enabled whole-lung DVC analysis in healthy and diseased mouse lungs, revealing heterogeneous strain distributions associated with altered airway integrity and ventilation-induced mechanical burden (Arora et al., 2024). These studies effectively showed the high potential of DVC computation for regional lung strain measurement. However, all of these DVC computations were based on HR synchrotron radiation microCT data, which require access to specialized facilities, involve constrained experimental conditions, and impose high radiation doses, thereby limiting their broader applicability toward animal studies on lung diseases. Extending DVC-based strain measurements to laboratory microCT data would significantly broaden accessibility and enable new strain analysis applications without reliance on synchrotron facilities. The detailed evaluation of DVC settings and imaging parameters for accurate regional strain measurement in soft tissues, particularly lungs, that would enable these applications, is currently lacking.

Therefore, the aim of this study was to investigate how lung microstructure, imaging quality, deformation magnitude, and DVC analysis parameters influence the accuracy of regional strain measurements. We assessed, both quantitatively and qualitatively, the effects of DVC operational parameters, lung microstructure, and quality of the imaging data including noise level and voxel size, on accuracy of strain measurements using DVC based on HR CECT data. We started with HR CECT data with high image contrast, which exhibited different levels of background attenuation between the datasets due to the different immersion media used for the samples. The imaging data were then exposed to different noise levels and larger voxel sizes to assess the accuracy of DVC under challenging imaging conditions. Different operational parameters in DVC, such as subvolume size (local DVC) and mesh size (global DVC), deformation magnitude range between the reference and deformed volumetric images, and quality of the registration were studied. Thereto, we assessed the feasibility of using DVC to quantify strain from HR *ex vivo* CECT data, determine the limits of measurement accuracy, and evaluate its potential applicability to lower-resolution and noisier datasets, such as those obtained from HR *ex vivo* microCT.

2. Materials and methods

2.1. Samples preparation and staining process

Two healthy murine lung samples, as leftover organs repurposed from another study according to 4 R's, were acquired in compliance with national and European regulations and were approved by the animal ethics committee of KU Leuven (P083/2023). The lungs were stained with Hf-WD 1:2 POM, as a contrast-enhancing staining agent, that was synthesized in-house (Ginsberg, 2009; Pétré et al., 2024). Hafnium-substituted Wells-Dawson polyoxometalate (Hf-WD 1:2 POM)

was used as the contrast agent for CECT due to its ability to provide high soft-tissue contrast with minimal tissue shrinkage, preserving the native morphology of the lung tissue and enabling accurate 3D visualization and quantitative measurements (de Bournonville et al., 2020; Starovoyt et al., 2023). The CESA solution was prepared by dissolving 35 mg/mL of Hf-WD POM powder in PBS. This concentration was chosen as it was previously showed to yield sufficient soft-tissue contrast for CECT while maintaining physiological conditions and minimizing alterations to tissue morphology (Starovoyt et al., 2023). Each lung sample was immersed in 5 mL of staining solution for 10 days while placed on a horizontal shaker plate at room temperature. To avoid dehydration and movement of the samples during CECT acquisition, the samples were fixed to small plastic bars attached to the caps of centrifuge tubes. Sample 1 was immersed in Hf-WD POM and sample 2 was immersed in PBS.

2.2. CECT data acquisition

CECT scans were acquired using a Phoenix Nanotom M (GE Measurement and Control Solutions, Germany) equipped with a 180 kV/15 W energy nanofocus X-ray tube. The lung samples were scanned over a 360° scan (frame averaging = 3; image skip = 0) with a 0.2 mm aluminum filter and 2500 images were acquired using the following parameters: a 60 kV X-ray source voltage, 350 μA current, 500 ms exposure time, and 3.8 μm voxel size. The CECT datasets were reconstructed with the Datos|x software (GE Measurement and Control Solutions) and exported as XY slices (.tiff).

2.3. Data pre-processing

To produce deformed volumetric images with a global deformation for DVC-based strain analysis, synthetic deformation was applied to three ROIs in CECT data of each sample using transform sequence module in Avizo software (Version, 2021.1, Thermo Fisher Scientific, France). Using this module, deformations ranging from 5 to 30 voxels in the Y-direction were performed. Transform sequence module uses linear intensity interpolation to resample voxel intensities and preserve grey-scale continuity. The transformation was applied to the full ROI volumes while maintaining consistent image dimensions to ensure compatibility between reference and deformed datasets. This approach enabled the generation of controlled image pairs with known displacement fields for quantitative validation of the DVC pipeline.

To investigate the effect of voxel size on DVC computation, a ROI including 600 × 600 × 600 voxels from sample-2 was selected as the reference image. The reference image (3.8 μm voxel size) was binned into four datasets with voxel sizes ranging from 7.6 to 30.4 μm, using CTan (version 1.18.8, Bruker microCT). Voxel binning was performed by averaging the intensity values of neighboring voxels, reducing image noise while preserving overall intensity distribution. As the result of the binning process, the physical volume of the generated datasets remain the same, but the number of voxels decreased from 600 × 600 × 600 voxels in the reference image to 75 × 75 × 75 voxels in the Bin 8×8 dataset.

To assess the impact of noise in the imaging data on strain measurements using DVC, five noisy datasets with varying levels of Gaussian noise, ranging from 2.5 to 30 standard deviations (std) were synthetically generated by adding varying levels of noise to the reference and deformed datasets in ImageJ.

To produce a volumetric image with a regional deformation, we applied a twist, with a 30° rotation to define the magnitude of the twist, in a circular ROI in the middle of the binning reference datasets in GIMP software (V3.0.4, the GIMP development team), using wrap transform module. This magnitude of the twist (30° rotation) was chosen arbitrarily to generate a sufficiently large spatial deformation field for a qualitative assessments.

2.4. Image analysis

We measured the quality of the imaging datasets with signal to noise ratio (SNR) and contrast ratio (CR) over small ROIs in each sample containing homogeneous lung tissue without large airways or blood vessels. Lung and background (air) signals and their standard deviations (STD) were measured over these ROIs using a semi-automatic density-based thresholding with a user-defined threshold value in CTan. The mean voxel intensity of the segmented lung tissue was used as the lung signal, while the mean voxel intensity and standard deviation of segmented air regions within the lung structure were used as the background signal and background STD, respectively. SNR and CR were measured using the following formulas (Goerner and Clarke, 2011; Pelli and Bex, 2013):

$$SNR = \frac{Lung\ signal}{Background\ STD}$$

$$CR = 2 \times \frac{(Lung\ signal - Background\ signal)}{Lung\ signal + Background\ signal}$$

Lung porosity and tissue thickness distribution were measured at multiple ROIs in each lung sample using CTAn. Porosity was calculated as the ratio of airway volume to total volume using semi-automatic threshold-based segmentation. For thickness measurement, CTAn employs a sphere-fitting algorithm that determines the largest possible sphere that fits entirely within the structure and contains each voxel.

2.5. Digital volume correlation (DVC)

All DVC computations in this study were conducted using Avizo software (Version, 2021.1, Thermo Fisher Scientific, France). DVC was applied to the reference and deformed data to generate 3D full-field displacement and strain maps of the lung samples. DVC offers two approaches for displacement and strain measurements: a traditional subset-based method known as the local approach, and a more robust finite element-based method called the global approach. The local DVC approach relies on dividing the reference and deformed volumetric images into smaller subvolumes, which are individually correlated. The global DVC technique assumes a continuous measured displacement field, enabling more accurate and robust results. However, it relies on a fine hexahedral mesh, which increases computational cost. We used a hybrid approach combining both local and global methods, in accordance with the Avizo tutorial guidelines and as previously described (Tozzi et al., 2014). Similar hybrid workflows combining local DVC for initial displacement estimation followed by global finite element-based refinement have been widely reported in previous studies (Tozzi et al., 2014; Roux et al., 2008). For the local DVC approach, subvolumes with varying sizes, 60, 120, 150, 200, 300 and 600 voxels, were used to assess their impact on image registration. The settings were configured to account for both translation and rotation in the transformation process, with the correlation threshold set at 0.7. This value corresponds to the default setting in Avizo DVC and is user-dependent and analysis-specific, influencing the trade-off between measurement uncertainty and spatial coverage of the resulting displacement field. The algorithm iteratively determined the six parameters, three translations and three rotations, of a rigid transformation matrix that best aligns the gray-level intensities of the reference and deformed images. For the global DVC computation, the same range of subvolume sizes used in the local DVC was applied to define cell sizes and generate the computational meshes. The displacement field of the local DVC was used as the initial displacement field for global DVC computation. To solve the finite-element equations, the maximum number of iterations was set to 300, and convergence criterion to 0.001. A maximum of 300 iterations and a convergence criterion of 0.001 were used, in accordance with standard settings in Avizo's finite-element-based DVC implementation. These values are commonly adopted to ensure convergence of the

iterative solver while limiting computational cost, with the convergence threshold providing sufficient numerical accuracy for stable displacement field reconstruction.

3. Results

3.1. Lung microstructure and image quality vary across lung samples and imaging datasets

The characteristics of the lung samples and imaging datasets were evaluated by assessing variations in lung microstructure and image quality. The DVC algorithm relies on greyscale patterns within samples to register reference and deformed images and to ensure accurate strain measurement. Since these greyscale patterns are directly influenced by the underlying tissue architecture, variations in lung microstructure may affect the reliability and accuracy of DVC-based strain measurement. We assessed the effects of microstructure not only between samples but also within each individual sample, since the ROIs were selected from different areas of the lung samples with varying tissue microstructures. We measured tissue thickness distribution *per* ROI in each sample (Supplementary Fig. 1), average tissue thickness and porosity *per* ROI of the both lung samples (Fig. 2-Panel B). The lung thickness distribution analysis revealed that sample 1 (S1) contained smaller lung structural features (3.8-11.4 μm), whereas sample 2 (S2) was characterized by larger features (11.4-19 μm). Moreover, lung features in the 3.8–11.4 μm range accounted for approximately 8% of the total volume in S1, whereas this size range was absent in S2, and features in the 11.4–19 μm range accounted for less than 1% of the total volume. Differences were observed not only between the two samples but also among the ROIs within each sample, based on both tissue thickness and porosity (Fig. 2- Panel B). The CECT dataset of S2 visually showed less noise and a clearer distinction between lung tissue and air compared to S1 (Fig. 1), which resulted in a higher CR for S2 compared to S1 (Fig. 2-Panel C). This difference could be attributed to the different immersion media used during CECT scanning which led to higher background attenuation for S1 since it was submerged in contrast agent, while S2 was submerged in PBS. However, the SNR was higher for S1 compared to S2, since the background STDs were nearly identical while the lung signal for S1 was higher than S2. These results indicated that the lung samples differed both in their microstructural characteristics, specifically lung feature size and its distribution, and in overall image quality. The impact of these parameters on image registration, strain measurement and the differences between the datasets were subsequently investigated.

3.2. Image registration is influenced by deformation magnitude, subvolume size, and mesh size

This section evaluated the effects of key parameters, including deformation magnitude, subvolume size, and mesh size, on the accuracy of image registration. All of the DVC computations with different conditions in this study reached convergence within 300 iterations, reaching a residual of 0.001. However, the number of iterations required to achieve convergence varied among the mesh sizes. Both very small and very large meshes generally required more iterations to converge, whereas intermediate mesh sizes reached convergence more rapidly. In the local DVC approach, a similarity metric ranging from 0 (poor correlation) to 1 (strong correlation) is assigned to each subvolume, with the mean metric representing the average similarity across the volume of interest. In the global DVC approach, the displacement field is obtained by minimizing intensity differences between the reference and deformed images, and correlation residuals quantify the remaining intensity mismatches. Residuals with values close to zero indicate that the displacement field accurately represents the deformation, whereas larger residuals suggest reduced agreement between the reference and deformed states.

The local approach was employed to capture an initial displacement field on coarse subvolumes, which was then used to initialize the global DVC approach using a finite element-based technique with a fine mesh. After each DVC computation, the quality of registrations between the reference and deformed volumetric images was assessed using the mean metric value for the local DVC and correlation residuals for the global DVC. The size of the defined subvolumes in local DVC and the mesh in global DVC can directly influence the accuracy of the results. Therefore, to prevent under- or over-estimation of the computed displacement and strain fields, we optimized the subvolume and mesh sizes based on mean metric values for local DVC and correlation residuals for global DVC, over a range of deformations between the reference and deformed images. We measured the mean metric and correlation residual values at different subvolume sizes, ranging from $60 \times 60 \times 60$ to $600 \times 600 \times 600$ voxels. This range divides the volume of interest into 1, 8, 27, 64, 125 and 1000 subvolumes, covering a wide range of subvolumes. We used synthetic deformation to produce deformed images (Fig. 3), ranging from 5 to 30 pixels in the Y direction.

Mean metric values for both samples showed a strong effect of subvolume size and deformation on image matching between the reference

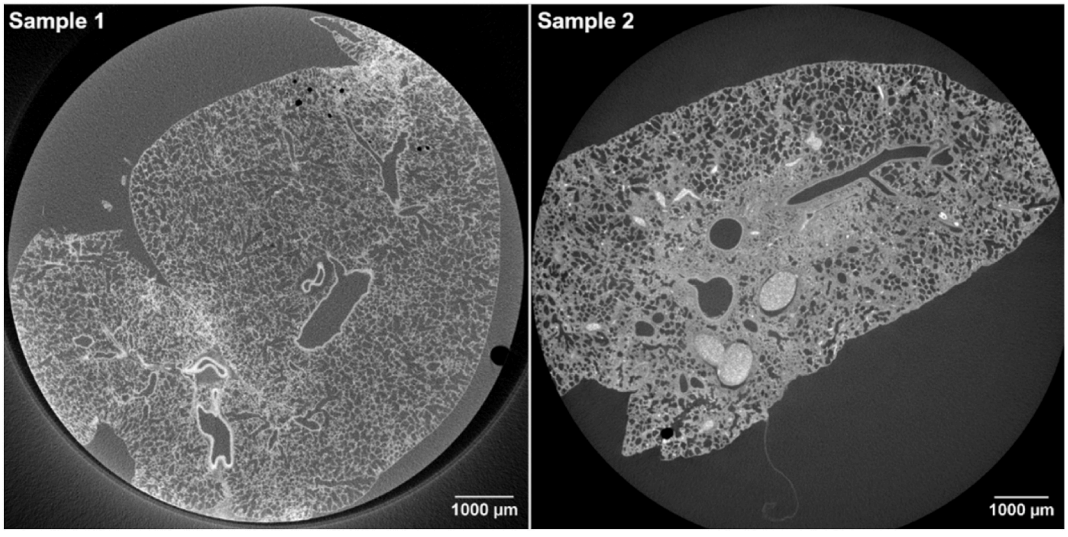

Fig. 1. CECT cross-sectional images of two murine lung samples stained with Hf-WD POM. CECT scans for both samples were acquired using a Phoenix Nanotom M. Sample 1 (left) was immersed in Hf-WD POM in a centrifuge tube during the CECT scanning. Right: Sample 2 (right) was immersed in PBS.

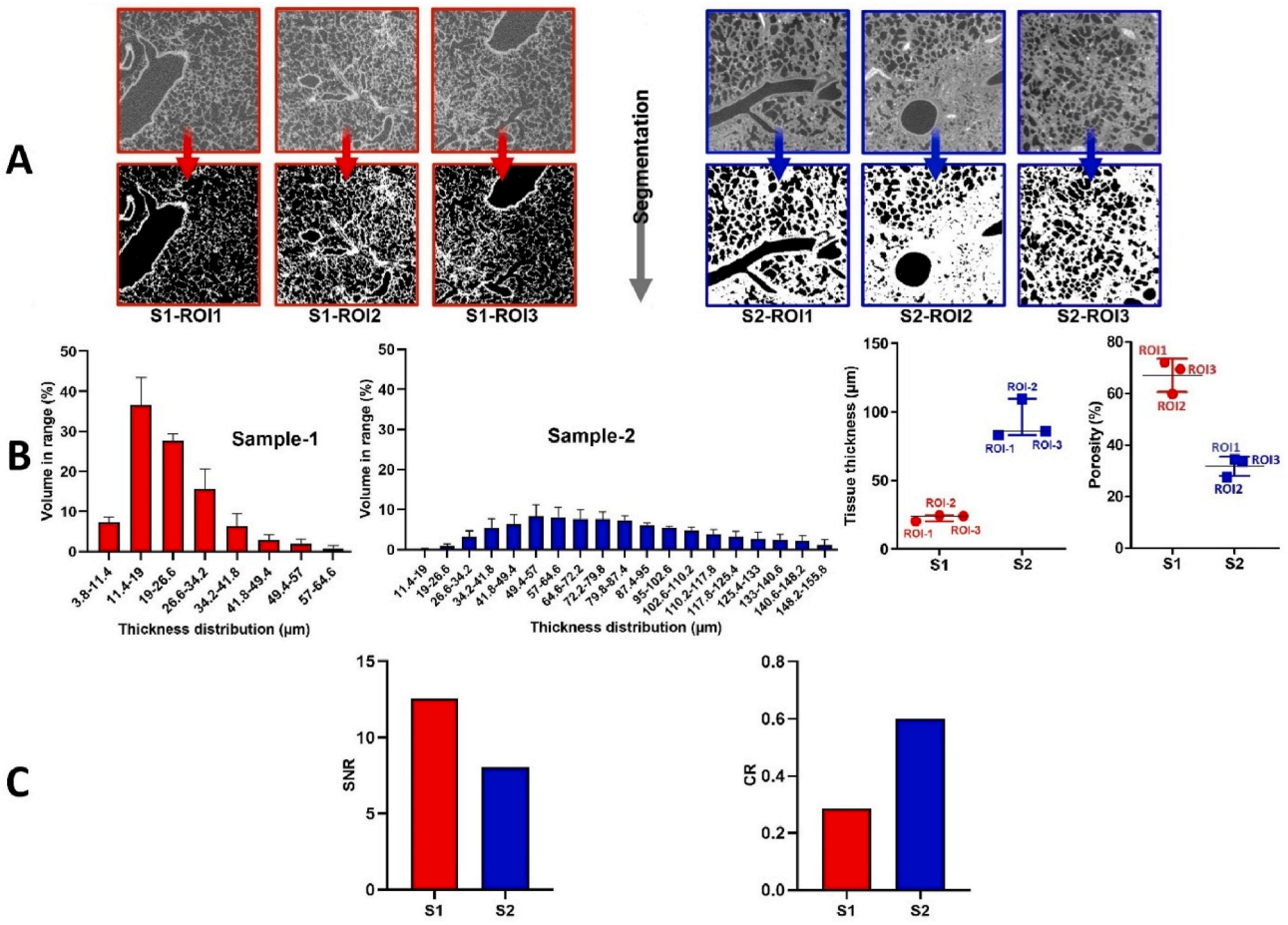

Fig. 2. *Variations in lung microstructure and image quality between the lung samples. (A) Three ROIs per sample were selected and segmented using density thresholding for microstructural and image quality analyses. (B) Tissue thickness distribution per sample, average tissue thickness per ROI and porosity were measured for three ROIs in each sample based on segmentation of the lung tissues. The standard deviations in tissue thickness distributions show variations between ROIs in each sample Average tissue thickness and porosity are presented per ROI, as well as the median with interquartile range per sample. (C) Image quality of the CECT datasets are checked based on SNR and CR. The higher CR in S2 compared to S1 explains the greater visual contrast between lung tissue and background. S1 exhibited higher background attenuation compared with S2, as it was immersed in the contrast agent during CECT acquisition, whereas S2 was immersed in PBS.*

and deformed images (Fig. 4). For S1, with a certain deformation, mean metric values generally decreased with increasing subvolume size. For large deformations, ranging from 3.3% to 5% (20 to 30 voxels), the mean metric values increased with increasing subvolume size from 60 to 120 voxels. With a 0.8% (5 voxels) deformation and a subvolume size of 60 voxels, the mean metric value was close to 1, indicating good matching between the reference and deformed images. As the deformation increased, the mean metric value decreased, indicating weaker image matching. A similar trend was observed for the other subvolume sizes in S1. For S2, a comparable trend was observed, though with a smaller effect of both subvolume size and deformation on mean metric values compared to S1. To minimize computational cost in local DVC computation, we selected the largest subvolume size with a high mean metric value, 200 voxels, which showed only minimal differences compared to the smaller subvolume (150 voxels). The results from the global DVC were obtained using the displacement field from the local DVC, computed with the optimal subvolume (200 voxels), as the initial input for the global DVC computation. Regarding the correlation residuals, mesh sizes ranging from 60 to 150 voxels showed minimal values, very close to zero, for S1 regardless of the deformation. Therefore, we selected 150 voxels, the largest mesh size that resulted in the minimum correlation residuals, as the optimal mesh for the global DVC computation for S1. The optimal mesh size for S2 was 200 voxels, representing the largest mesh size that yielded the minimum correlation residuals. The difference in optimal mesh size between S1 and S2 could be due to differences in lung feature size and their spatial distribution (Fig. 2, Panel B). Specifically, S1 exhibited smaller features, which require a finer mesh to accurately capture local deformations and achieve reliable registration between the reference and deformed images. In contrast, the larger feature sizes in S2 allowed for accurate registration with a comparatively coarser mesh.

3.3. Multiple factors influence the accuracy of DVC-based strain measurements between the two samples

The accuracy of DVC-based strain measurements was assessed using the two datasets to identify differences between the samples and the factors affecting measurement accuracy. Global strain measurements were performed for each sample using its optimal subvolume (200 voxels) and mesh sizes (150 voxels for S1 and 200 voxels for S2), determined from the image matching metrics and the previously applied linear synthetic deformation. The ground-truth strains corresponding to the synthetic deformations were used to calculate relative errors and evaluate the accuracy of the DVC outputs (Fig. 5). Strain measurements for S1 showed that at 0.8% deformation (5 voxels), the mesh size had a minor effect on the strain measurement up to a mesh size of 300 voxels, with acceptable relative errors (less than 6%). The 600 voxels mesh size here means the whole volumetric image as one mesh, which explains the high inaccuracies for strain measurement for this mesh size. The effect of mesh size on strain measurement became more pronounced as the

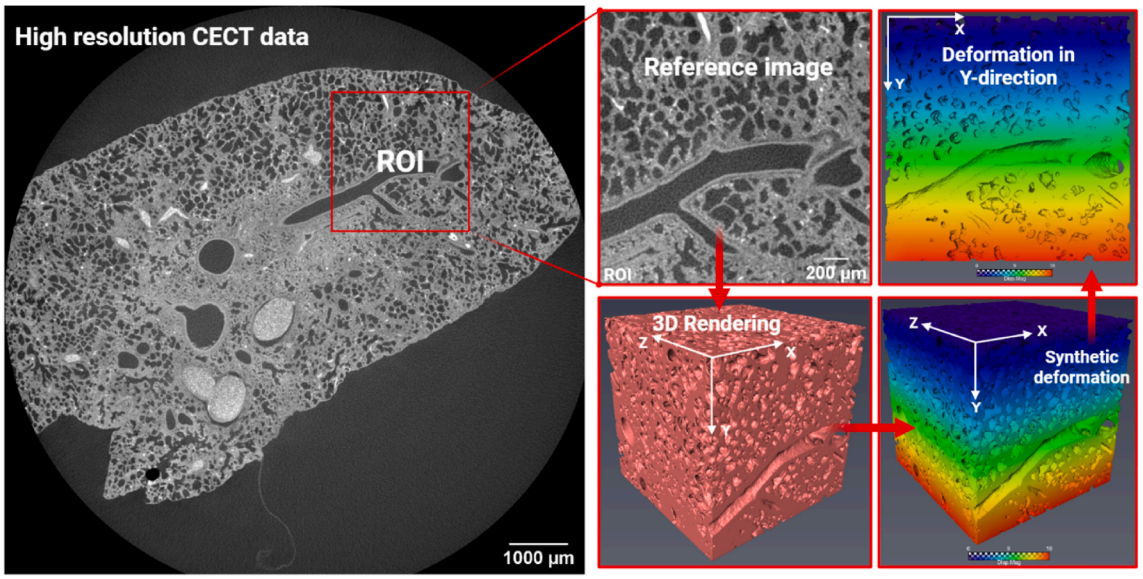

Fig. 3. Generation of deformed datasets synthetically for assessing DVC accuracy. Synthetic deformation in the Y-direction with different magnitudes was applied to generate deformed volumetric images with known values for optimizing DVC parameters based on accuracy of DVC outputs. Left: a small volumetric ROI within sample-2 was selected and used as the reference image, from which deformed images at varying magnitudes were produced using the Transform Sequence module in Avizo. The top-right image shows a linear deformation along the Y-axis, with minimum deformation at the top (blue) and maximum deformation at the bottom (red).

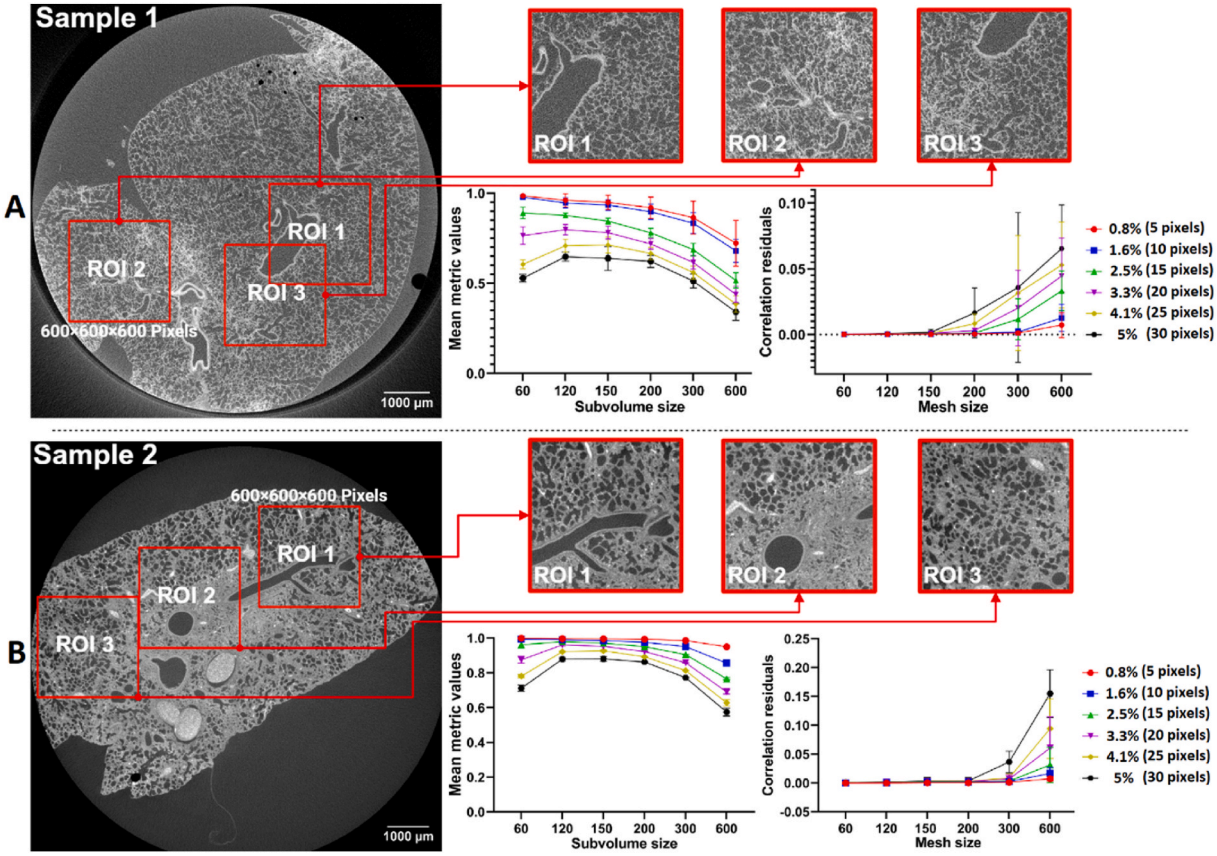

Fig. 4. Determination of optimal subvolume and mesh sizes using registration metrics of local and global DVC: (A) Graphs from DVC computations using CECT data of sample-1: left graph shows mean metric values versus subvolume size for local DVC, and right graph shows correlation residuals versus mesh size for global DVC. Standard deviations indicate variability across the ROIs in sample-1. A subvolume size of 200 voxels yielded a high mean metric value with a minimal difference compared to 150 voxels, making it the optimal choice for local DVC. A mesh size of 150 voxels resulted in the lowest correlation residuals, similar to 120 voxels, representing as the optimal choice for global DVC. (B) Panel B shows the same graphs for sample-2. For this sample, both local and global DVC are optimized at a subvolume and mesh size of 200 voxels.

deformation magnitude increased, leading to higher relative errors compared to the ground-truth strains. For large deformations (4% and

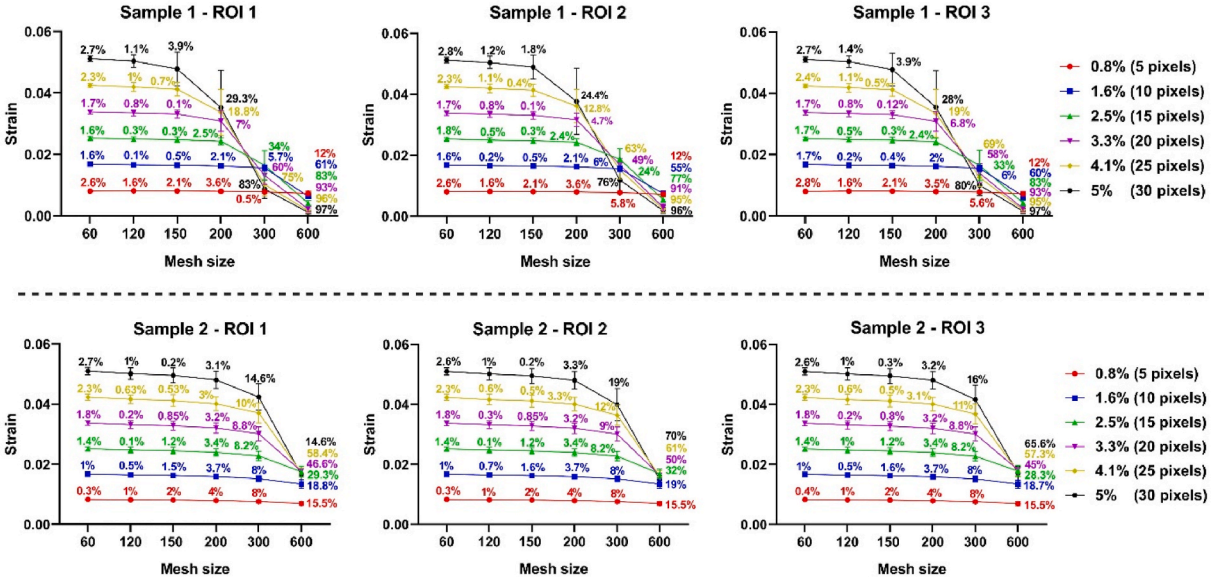

Fig. 5. Global strain measurements using the hybrid DVC approach and CECT data of two lung samples. DVC computations were performed on synthetically deformed images with known deformations along the Y-axis, ranging from 5 to 30 pixels (0.8–5%). Each graph shows strain versus mesh size, with data points representing the average strain from three repeated DVC computations at each mesh size. Error bars indicate standard deviations, reflecting variability across the repetitions. Percentages above each data point represent the relative error between the ground-truth synthetic deformation and the DVC outputs. For sample-1, the optimal and smaller mesh sizes (≤150 voxels) measured the ground-truth strain values with high accuracy. The same trend was observed for the optimal and smaller mesh sizes (≤200 voxels) for sample-2.

5%), sharp declines in the accuracy of strain measurements were observed between mesh sizes of 150 and 200 voxels. Regardless of the deformation values, mesh sizes of 60, 120, and 150 voxels, the optimal mesh size and smaller meshes, yielded high accuracy strain measurements across all ROIs of S1, with relative errors of less than 4%. For S2, the trend in strain values is similar to that of S1, where the accuracy of strain measurements sharply declined for large deformations (4% and 5%) beyond the optimal mesh size for this sample as well, which was 200 voxels. Strain measurements across different ROIs of the same sample confirmed that mesh sizes of 150 and 200 voxels were optimal for S1 and S2, respectively. This finding was consistent with what the correlation residuals indicated in the previous section. Therefore, accurate strain quantification at high deformation magnitudes (up to 5% between reference and deformed images) was possible upon selecting an optimal, sample-specific mesh size.

Although the effects of mesh size and deformation on strain measurement followed the same trend for both samples, the drop in accuracy of the strain measurements using DVC was more pronounced at large deformations (4% and 5%) for S1 compared to S2. The first sharp drop occurred between mesh sizes of 150 and 200 voxels for S1, whereas for S2, it occurred between 200 and 300 voxels. For S1, at the highest deformation (5%), the relative error for the mesh size of 150 voxels was around 4%, increasing to nearly 30% for the mesh size of 200 voxels. However, for S2, at the same deformation magnitude, the relative error for the mesh size of 200 voxels started at around 3% and increased up to 19% for mesh size of 300 voxels, showing a less sharp drop in DVC accuracy compared to S1. These findings may reflect differences in image quality and underlying lung microstructure between the samples (Fig. 2), which appeared to affect the correlation residuals and the determination of optimal mesh sizes. The following sections examine the parameters that may influence the accuracy of the DVC output further.

3.4. Imaging noise level influences strain measurement accuracy

To investigate the impact of noise on strain measurements with DVC, while keeping the lung microstructure and imaging voxel size constant, we exposed ROI1 of S2 to different levels of synthetic Gaussian noise, creating noisy datasets. We examined the impact of noise levels in the imaging data at different deformation magnitudes using synthetic deformation, as explained previously. The synthetic noise was applied to the deformed datasets after the synthetic deformation process. The highest level of applied noise (20 std) did not result in a visually noticeable difference in the clarity of the lung microstructure compared to the reference image (Fig. 6, panel A). However, the effects of these synthetic noise levels were evident in the SNR values with a decreasing trend (Fig. 6, panel B). The CR values showed minimal variation among the noisy datasets. We performed global DVC computations for strain measurements on the noisy datasets at different mesh sizes and varying deformation magnitudes, ranging from approximately 1-3% (Fig. 6, panel C). All global DVC computations were performed using initial displacement fields derived from local DVC computations with the optimal subvolume size. For mesh sizes smaller than the optimal size (200 voxel size), the effect of noise levels on the accuracy of strain measurements was limited to 6% relative error up to the noise level of 5 std. For higher noise levels, sharper drops in accuracy were observed. As the mesh size increased beyond the optimal value, the effect of noise on strain measurements became more pronounced, resulting in higher relative errors. Similarly, increasing the deformation heightened the impact of noise on the accuracy of strain measurements, particularly with mesh sizes larger than the optimal mesh. These results indicated that, with an optimal combination of mesh size and deformation magnitude, DVC can tolerate noise levels up to 5 std with reasonable accuracies.

3.5. Large voxel sizes limit strain measurements

We investigated the role of imaging voxel size on regional lung strain distributions by synthetically increasing the voxel size of the CECT data. To generate images that only differ in voxel sizes, we used ROI1 of S2 volumetric image as the reference image and binned it into four additional datasets with progressively larger voxel sizes, ranging from 3.8 μm for the reference image to 30.4 μm for Bin 8×8 (Supplementary Fig. 2). Since the ultimate aim is to determine the limits of the potential application range in which regional lung strain distributions can be used

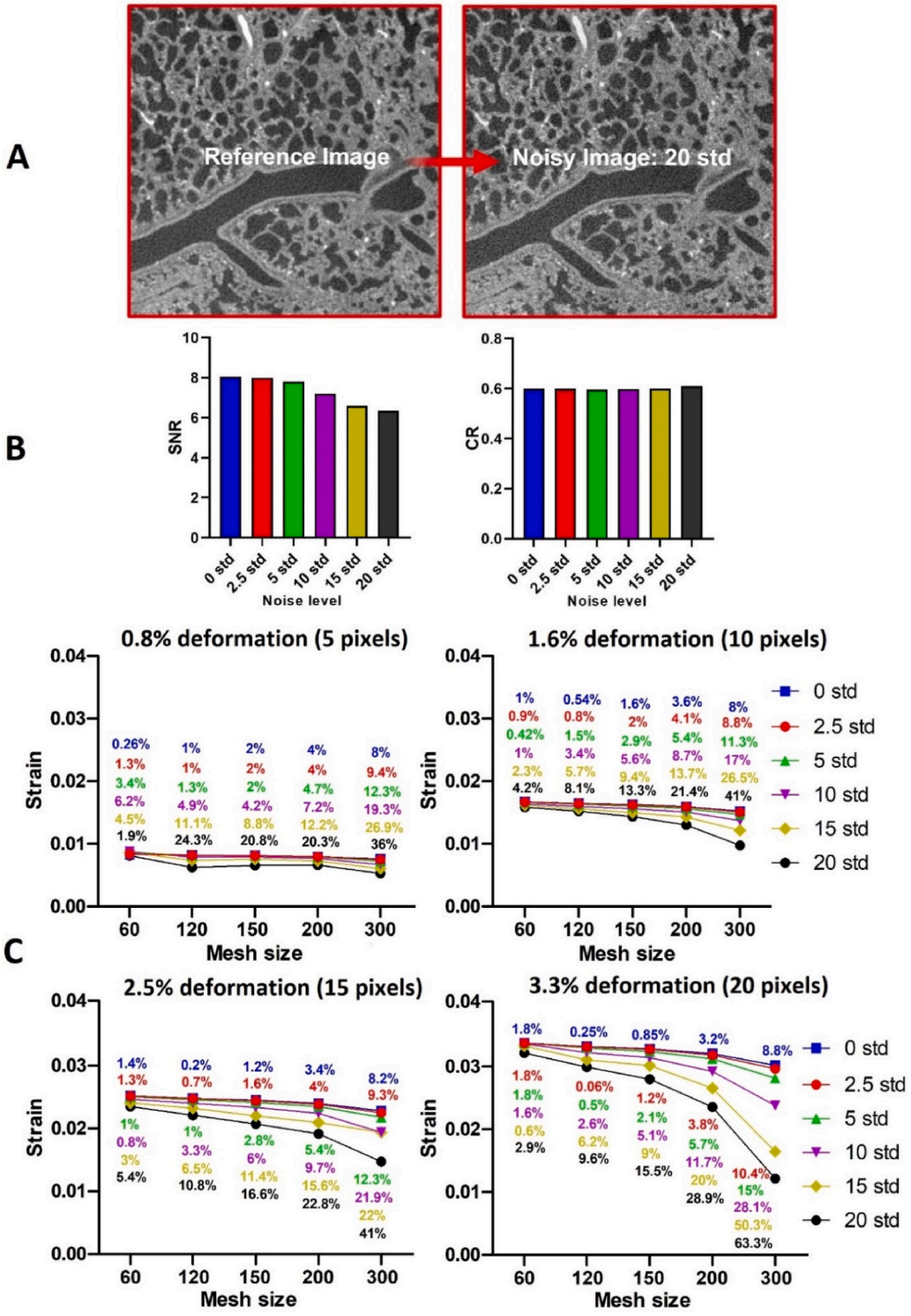

Fig. 6. Impact of varying imaging noise levels on DVC-based strain measurement accuracy. Strain measurements using DVC were performed on synthetically generated noisy datasets based on sample-2, ROI1 to study the impact of imaging data noise levels. **(A)** The highest level of applied noise (20 std) did not result in a visually noticeable difference compared to the reference image. **(B)** Synthetic noise slightly increased the CR values of the images while decreasing the SNR values. **(C)** The results showed a clear loss of accuracy in lung strain measurements using DVC as noise levels increased for a given mesh size and deformation magnitude. Moreover, the impact of noise was amplified with larger mesh sizes and greater deformation magnitudes.

to differentiate between healthy and diseased regions using *ex vivo* microCT data, we synthetically binned the CECT data to increase the voxel size up to 30.4 μm (Bin 8×8). This allowed us to investigate the impact of reduced image resolution under conditions similar to those encountered in *ex vivo* imaging datasets (Fig. 7, panel A). We qualitatively assessed the effect of voxel size of the imaging data on a regional lung strain distribution. To visually compare the regional strain distribution between the datasets with different image voxel sizes, normal strain components in X, Y and Z directions were computed. The regional strain distribution of the reference image (3.8 μm voxel size)

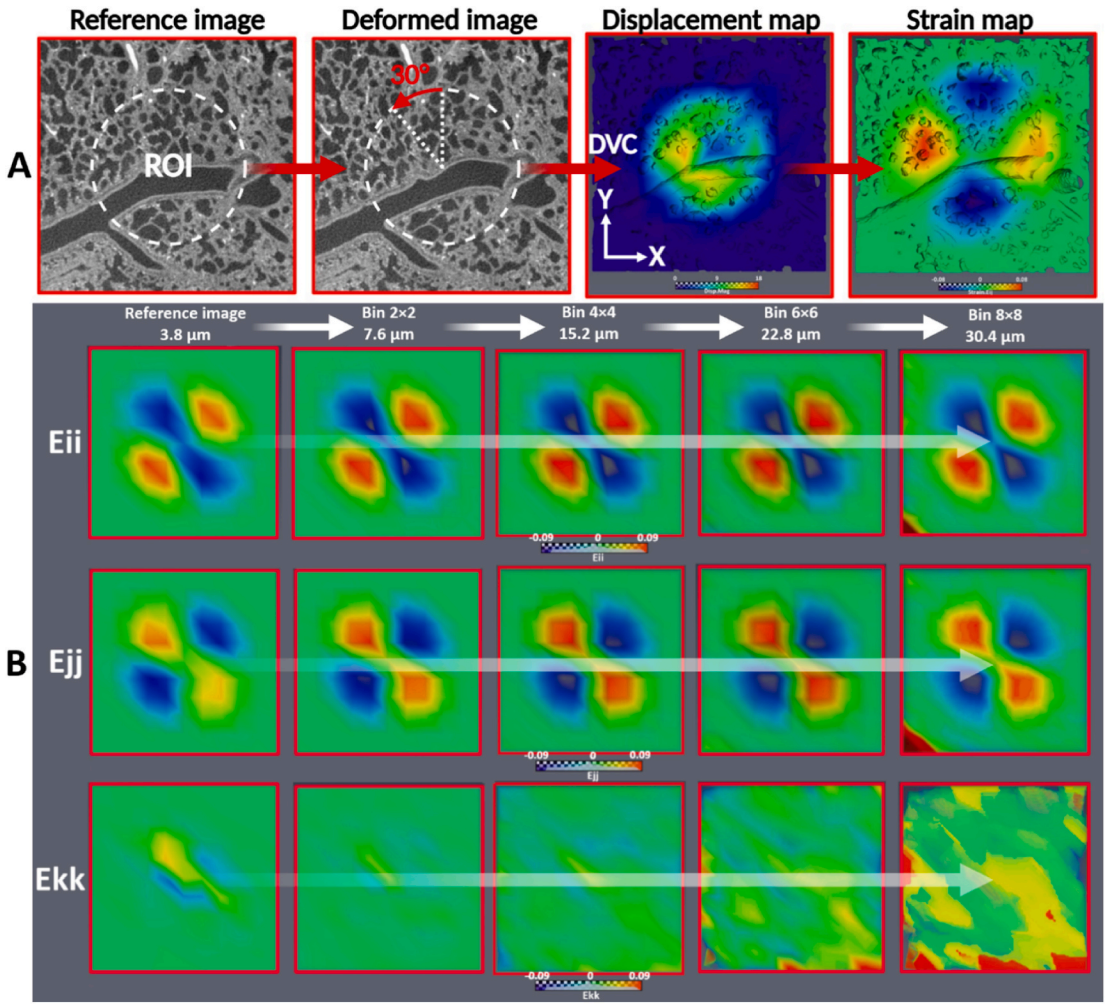

Fig. 7. Evaluation the role of voxel size of the imaging data on regional lung strain distribution. **(A)** A circular ROI was selected in ROI-1 of the sample 2 to induce a regional deformation using a 30° twist. The regional displacement and strain distribution are shown for the reference dataset (3.8 µm). **(B)** Normal strain components in X (Eii), Y (Ejj) and Z (Ekk) directions were computed and visualized for the binned datasets. The range of the strain distribution in each strain component was kept the same between the datasets to make the strain distribution comparable and is shown below each row. This strain distribution at each component remains almost the same by increasing the voxel size from 3.8 µm to 22.8 µm. In Bin 8×8, with voxel size of 30.4 µm, boundary errors appeared as high intensity areas in red in the border of the images.

served as the ground truth in our comparison. Considering the Eii component, normal strain component in X direction (Fig. 7, Panel B, first row), the strain distribution remained almost the same when increasing the voxel size to 22.8 µm (Bin 6×6). Increasing the voxel size to 30.4 µm (Bin 8×8), did not altered the regional strain distribution. However, a high intensity strain region appeared in the bottom left corner of the volumetric image that was absent in previous datasets, including the ground-truth dataset. This high-intensity strain region represented a boundary error in the DVC computation. The regional strain distribution with normal components in Y and Z directions, Ejj and Ekk respectively, remained almost unchanged similarly to Eii up to the voxel size of 22.8 µm (Bin 6×6). Boundary errors were visible for Ejj and Ekk, similar to Eii, for the voxel size of 30.4 µm (Bin 8×8). Strain distribution in Z direction, Ekk, was different from Eii and Ejj since the initial deformation was applied to XY plane. Visual representation of the strain distributions in 3D showed that boundary errors happened even in lower voxel sizes, down to 15.2 µm in Bin 4×4 (Supplementary Fig. 3).

Considering the shear components of the strain matrix, strain components in YZ and XK planes (Eij, Eik, and Ejk), a similar trends were observed compared to the normal strain components, where the local strain distribution in the reference image remained almost the same up to the Bin 6×6 (Supplementary Fig. 4). Boundary errors as new high intensity strain regions emerged in the bottom-left corner of the images. Since the initial deformation was applied to the XY plane, only the Eij component showed a clear strain distribution among the shear components. To further investigate the effect of voxel size on regional strain distribution with a different greyscale pattern, the same regional deformation was applied to a different ROI of the same lung sample with smaller feature sizes (i.e., without any large airway) to generate a deformed dataset. The resulting DVC-based regional strain distributions exhibited the same trends for both normal and shear strain components (Supplementary Fig. 5). This indicated that with small voxel sizes (below 15 µm), the same strain distribution could be consistently preserved. However, larger voxel sizes in the imaging data could impact the strain distribution using DVC through generating boundary errors. For voxel sizes above 15 µm, the volume of interest must be large enough (at least equal to radius of the ROI) to ensure that boundary errors do not affect regional strain measurements in the central region of the image.

4. Discussion

This study assessed the potential of DVC for accurate lung strain measurement using HR CECT data and evaluated the robustness of the framework to image quality degradation by investigating the effects of

increased noise levels and larger voxel sizes. For the first time using CECT data of mouse lung tissue, we examined the influence of several key parameters on DVC performance, including operational parameters of DVC, lung microstructure and image quality, including noise level on global strain measurements. Furthermore, we investigated the effect of imaging voxel size on regional strain measurements. Our findings showed the robustness of DVC-based strain measurements under challenging imaging conditions, with increased noise levels and larger voxel sizes, supporting the potential translation of this framework across a range of high-to lower-resolution datasets comparable to those encountered in HR *ex vivo* microCT imaging. While DVC has been widely used for strain analysis in bone (Dall'Ara and Tozzi, 2022), this work is among the few to explore its application in soft tissue such as the lung (Mazy and Kerckhofs, 2025; Arora et al., 2017, 2021, 2024). By demonstrating robust strain measurements under degraded imaging conditions, this study extends the potential applicability of DVC-based lung strain analysis beyond HR synchrotron microCT data toward the image quality achievable with HR *ex vivo* microCT.

Previous studies have shown that accurate DVC-based displacement and strain measurements depend heavily on image feature size and distribution and input image quality (Mazy and Kerckhofs, 2025; Dall'Ara and Tozzi, 2022; Comini et al., 2019b). It has been shown that DVC precision varies significantly among bones with different degrees of microstructural heterogeneity, with more heterogeneous tissues yielding higher precision at finer spatial resolutions. Additionally, computational parameters such as subvolume size in local DVC and mesh size in global DVC directly affect algorithm accuracy and precision. In a verity of bone samples, DVC precision improved with larger subvolumes or meshes regardless of bone type, but decreased with *in vivo* or synchrotron microCT data due to factors such as voxel size and noise (Dall'Ara et al., 2017). Furthermore, previous studies have shown that complex and nonuniform local deformation within a large subvolume or mesh can induce considerable systematic errors in displacement and strain measurements, thereby reducing accuracy (Pan and Wang, 2020). Consistent with these findings, the present study showed that, beyond certain subvolume and mesh sizes, the accuracy of strain measurements decreased sharply, with different behaviors observed depending on sublocation in lung, varying with the underlying lung microstructure. Introduction of new parameters, such as the ratio of the smallest feature size to mesh size, may help better quantify the influence of microstructural characteristics on the accuracy of DVC measurements in future studies. These findings altogether highlight a trade-off between precision and accuracy in DVC, in which increasing subvolume or mesh size improves precision, but may reduce accuracy when local deformation becomes complex or nonuniform. To the best of our knowledge, there have been no reports of comparable investigations in soft tissues, particularly the lung, to date. This study addresses that gap by assessing DVC accuracy in mouse lung tissue under synthetic deformations of varying magnitudes, using a hybrid approach: local DVC for initial displacement and strain fields, refined by global DVC for enhanced accuracy. The synthetic deformation applied here was not intended to replicate the complex mechanics of respiratory motion. Instead, it was designed as a controlled benchmark with known ground-truth displacement and strain fields, enabling a systematic evaluation of DVC parameter sensitivity and performance under well-defined deformation conditions.

To evaluate the performance of the hybrid DVC approach, the influence of subvolume and mesh size on registration accuracy was examined across deformation magnitudes and lung samples scanned in different immersion media. The mean metric value, serving as the registration metric for local DVC, was strongly influenced by subvolume size across deformation magnitudes. Both excessively small and large subvolumes reduced the mean metric value in both lung samples: small ones lacked sufficient identifiable features for accurate registration, whereas large ones violated the uniform displacement assumption due to spatial heterogeneity in the local displacement and strain fields. Subvolume-to-image volume ratios of 0.2, 0.25, and 0.33 performed similarly at each deformation magnitude. Thus, the largest was selected to reduce computational cost. Increasing deformation magnitude lowered the mean metric value, with more pronounced effects in very small and large subvolumes in S1 compared to S2, reflecting differences in microstructure, imaging quality, and noise. In global DVC, correlation residuals revealed different optimal mesh sizes for S1 and S2. Exceeding these sizes increased correlation residuals, as larger elements failed to capture local displacement variations. This study demonstrates that mesh size involves a fundamental trade-off between spatial resolution and measurement robustness. While small meshes capture fine structural details but are more susceptible to noise and correlation errors, overly large meshes smooth local deformation gradients and reduce registration accuracy, making an optimal mesh size essential for reliable DVC-based strain measurements. It is important to note that the results of this study do not define a general optimal mesh size for soft tissues or specifically for lung tissue. Instead, this study emphasizes key factors influencing accurate DVC-based strain measurements in soft biological tissues, particularly the lung, which remain underexplored in the current literature. Determining an optimal mesh size for a given lung sample undergoing complex deformation requires a DVC uncertainty measurement (zero-strain test) across multiple mesh sizes. This approach enables identification of the optimal mesh size that minimizes displacement and strain uncertainty and maximizes DVC precision for a specific combination of lung microstructure, deformation magnitude, and imaging quality, including voxel size, imaging artefacts, and noise level. Here, both DVC methods showed that deformation magnitude also critically influence registration accuracy between the reference and deformed images. Global strain measurements showed that DVC accuracy declined sharply at 5% deformation for mesh sizes of 150 (S1) and 200 (S2), aligning with the rise in correlation residuals. For mesh sizes yielding minimal residuals, relative errors across deformation magnitudes and ROIs remained within 4% for both samples. This supports the use of correlation residuals as a reliable indicator of registration quality in global DVC, ensuring robust strain measurements when minimized.

These results prompted further analysis of how intrinsic tissue characteristics, particularly microstructural features, contribute to variations in DVC accuracy. Studies on bone have shown that DVC accuracy and precision depend on tissue microarchitecture (Dall'Ara et al., 2017; Liu and Morgan, 2007b; Zhu et al., 2016). Up to threefold difference in strain error across trabecular bone types has been reported, with DVC error correlating with microstructural metrics, such as bone volume fraction and trabecular thickness (Liu and Morgan, 2007b). Using the ratio of subvolume size to microstructural spacing as a guide has been shown to reduce uncertainty when the ratio ranges from 1.6 to 4 (Zhu et al., 2016). In our study, microstructural differences also appeared to influence optimal DVC parameters. Although global strain trends were consistent within samples, small variations in relative error were observed, especially at mesh sizes exceeding the optimal. These differences may reflect underlying microstructural features, such as the presence of a large airway within the ROI. A more detailed investigation using lung samples with distinct microstructures and greyscale textures is needed to better understand these effects. In addition to tissue microstructure, image quality and associated artefacts can further influence DVC performance and measurement reliability (Paraskevoulakos et al., 2024; Croom et al., 2021). While common noise types were found to have minimal impact on DVC precision, severe artefacts such as ring artefacts introduced significant errors (Paraskevoulakos et al., 2024). In our study, the sample submerged in contrast agent (S1) during scanning produced noisier images than the sample submerged in PBS (S2). Therefore, the choice of submersion fluid may have indirectly influenced the DVC results through its effect on image noise levels, highlighting the importance of image quality for accurate image registration and reliable DVC-based strain measurements. Furthermore, increasing Gaussian noise consistently reduced DVC accuracy across all mesh sizes and deformation levels, with

stronger effects at higher deformations. Larger mesh sizes were more sensitive to noise, especially beyond the optimal size for each sample. These findings suggest that although DVC tolerates moderate noise, its accuracy declines with increasing noise, larger meshes, and greater deformation magnitudes. These results suggest that, with an optimal combination of mesh size, deformation magnitude, and voxel size, DVC can tolerate the noise without introducing significant inaccuracies.

Spatial resolution, determined by voxel size, represents another key factor influencing DVC accuracy (Dall'Ara et al., 2017; Liu and Morgan, 2007b; Palanca et al., 2017b). It has been shown that smaller voxel sizes enable low strain uncertainties with smaller measurement volumes, while down-sampling to larger voxels requires larger volumes to maintain accuracy due to loss of greyscale detail (Palanca et al., 2017b). In our study, down-sampling led to reduced DVC accuracy, especially at larger voxel sizes. Regional strain patterns in central regions remained consistent, suggesting that large voxel sizes (30 μm) can still yield reliable regional strain measurements, provided the analyzed volume is large enough to minimize boundary effects. Overall, despite limitations at the edges, DVC remains effective for capturing regional strain, supporting its potential application to HR *ex vivo* microCT data. Further investigation using a quantitative approach could complement this study. Moreover, although lung microstructure remained visible even at a voxel size of 30 μm with the binned datasets, this level of microstructural detail is not typically present in actual lung microCT datasets acquired at 30 μm voxel size. Therefore, actual datasets from the same sample scanned at multiple voxel sizes would help further confirm these findings.

Taken together, this study advances the application of DVC for strain analysis using HR CECT data of mouse lung tissue. Our findings have a direct impact on understanding how imaging quality, tissue architecture, and operational parameters of the DVC algorithm, under both local and global approaches, influence the accuracy of strain measurements in soft tissues. By addressing these interrelated factors in a highly complex organ such as the lung, this work provides a foundation for the reliability of DVC-based strain quantification in lung tissue using HR CECT, supporting its application as an endpoint approach for characterizing lung biomechanics with *ex vivo* microCT. Extending application of DVC to longitudinal *in vivo* microCT data remains considerably more challenging, as accurate image registration relies on stable and distinguishable anatomical features that can be compromised by respiratory and cardiac motion, image noise, reduced contrast, and dose considerations that all pose limits to the spatial resolution of *in vivo* imaging beyond voxel size alone. To the best of our knowledge, this study is the first to evaluate the potential of DVC-based strain analysis for assessing lung mechanics using HR CECT images subjected to varying lung microstructures and image quality conditions. Next steps in further unlocking the potential of DVC-based strain analysis, is to apply DVC to multiple *ex vivo* microCT data of healthy and diseased lungs for strain measurements to increase the sample size, at multiple stages of the breathing cycle, serving as actual deformed images building up to reflecting the full complexity of volumetric lung expansion under breathing motion rather than relying on synthetic deformations. Based on our findings and previous studies, the deformation magnitude between reference and deformed datasets should be limited to approximately 5%. To capture larger deformations, an incremental DVC approach can be employed, in which the total deformation is divided into multiple incremental steps rather than being measured in a single registration. However, the number of increments should be kept to a minimum to reduce the accumulation of errors across successive registration steps (Wang and Pan, 2018). In the present application, identifying disease-related strain distributions resulting from abnormalities such as fibrosis, which alter local tissue compliance, relies on the regional mechanical response and does not require analysis of the entire breathing cycle. The effects of imaging voxel size and noise level on strain measurements should be further investigated using experimentally acquired datasets of the same lung sample obtained at increasing voxel sizes, rather than relying on synthetically generated datasets. Repeating scans at the same stage of the breathing cycle would enable zero-strain tests to evaluate the precision of DVC in future work.

5. Conclusion

This study demonstrated the feasibility and potential of DVC-based strain analysis for investigating lung mechanics using HR CECT data of mouse lung tissue. We evaluated the influence of local and global DVC parameters, tissue microstructure, and imaging quality, including noise and voxel size, providing insights into the reliability and limitations of DVC in a highly compliant organ. Strain measurements in global DVC were highly sensitive to mesh size, with optimal meshes yielding robust estimates, whereas larger meshes reduced accuracy. Correlation residuals proved a reliable metric for selecting the optimal mesh size. Overall, these findings advance understanding of DVC-based strain measurements in soft tissues and provide a rational framework for microCT-derived biomarkers of lung biomechanics to advance lung disease and therapy studies.

CRediT authorship contribution statement

Kaveh Ahookhosh: Writing – review & editing, Writing – original draft, Visualization, Validation, Software, Methodology, Investigation, Formal analysis, Data curation, Conceptualization. **Grzegorz Pyka:** Methodology. **Lara Mazy:** Methodology. **Greet Kerckhofs:** Writing – review & editing, Supervision, Software, Project administration, Methodology, Conceptualization. **Greetje Vande Velde:** Writing – review & editing, Supervision, Project administration, Funding acquisition, Conceptualization.

Declaration of competing interest

The authors declare that they have no known competing financial interests or personal relationships that could have appeared to influence the work reported in this paper.

Acknowledgements

The X-ray CECT data were generated in the microCT lab of UCLouvain (Woluwe, IREC). Avizo 2024.2 (ThermoFisher Scientific, France) software acquisition was supported by the Fonds de la Recherche Scientifique-(FNRS - EQP - Tomo4D-U.N069.20). The authors thank Dr. Kamel Madi (3Dmagination Ltd.) for his valuable insights on DVC computation and data interpretation. This project was supported by a grant from KU Leuven Internal funds (C24E_23_036) and grants from the Flemish Research Foundation (G057721N, G0G4820N, I006524N).

Appendix A. Supplementary data

Supplementary data to this article can be found online at https://doi.org/10.1016/j.jmbbm.2026.107607.

Data availability

Data will be made available on request.

References

Ahookhosh, K., Gsell, W., Tielemans, B., Vande Velde, G., 2025. Respiratory rate as a X-ray-based biomarker for the longitudinal assessment of lung function and pathology. Front. Med. 12, 1621104.

Ahookhosh, K., Saidi, M., Mohammadpourfard, M., Aminfar, H., Hamishehkar, H., Farnoud, A., et al., 2021. Flow structure and particle deposition analyses for optimization of a pressurized metered dose inhaler (pMDI) in a model of tracheobronchial airway. Eur. J. Pharmaceut. Sci. 164, 105911. https://doi.org/10.1016/j.ejps.2021.105911.

Ahookhosh, K., Vanoirbeek, J., Vande Velde, G., 2023. Lung function measurements in preclinical research: what has been done and where is it headed? Front. Physiol. 14, 1130096.
Albers, J., Markus, M.A., Alves, F., Dullin, C., 2018. X-ray based virtual histology allows guided sectioning of heavy ion stained murine lungs for histological analysis. Sci. Rep. 8 (1), 7712.
Arora, H., Kernot, D., Giron, L., Howells, D., Darcy, M., Hoshino, M., et al., 2024. Lung disease characterised via synchrotron radiation micro-CT and digital volume correlation (DVC). TrAC, Trends Anal. Chem., 117588
Arora, H., Mitchell, R.L., Johnston, R., Manolesos, M., Howells, D., Sherwood, J.M., et al., 2021. Correlating local volumetric tissue strains with global lung mechanics measurements. Materials 14 (2), 2. https://doi.org/10.3390/ma14020439.
Arora, H., Nila, A., Vitharana, K., Sherwood, J.M., Nguyen, T.T.N., Karunaratne, A., et al., 2017. Microstructural consequences of blast lung injury characterized with digital volume correlation. Frontiers in Materials [Internet] 4 (41) [cited 2023 Jun 30]. Available from: https://www.frontiersin.org/articles/10.3389/fmats.2017.00041.
Berghen, N., Dekoster, K., Marien, E., Dabin, J., Hillen, A., Wouters, J., et al., 2019. Radiosafe micro-computed tomography for longitudinal evaluation of murine disease models. Sci. Rep. 9 (1), 17598.
Broche, L., Perchiazzi, G., Porra, L., Tannoia, A., Pellegrini, M., Derosa, S., et al., 2017. Dynamic mechanical interactions between neighboring airspaces determine cyclic opening and closure in injured lung. Crit. Care Med. 45 (4), 687–694.
Buljac, A., Jailin, C., Mendoza, A., Neggers, J., Taillandier-Thomas, T., Bouterf, A., et al., 2018. Digital volume correlation: review of progress and challenges. Exp. Mech. 58 (5), 661–708. https://doi.org/10.1007/s11340-018-0390-7.
Cercos-Pita, J.L., Fardin, L., Leclerc, H., Maury, B., Perchiazzi, G., Bravin, A., et al., 2022. Lung tissue biomechanics imaged with synchrotron phase contrast microtomography in live rats. Sci. Rep. 12 (1), 5056.
Chu, T., Ranson, W., Sutton, M.A., 1985. Applications of digital-image-correlation techniques to experimental mechanics. Exp. Mech. 25, 232–244.
Comini, F., Palanca, M., Cristofolini, L., Dall'Ara, E., 2019a. Uncertainties of synchrotron microCT-based digital volume correlation bone strain measurements under simulated deformation. J. Biomech. 86, 232–237.
Comini, F., Palanca, M., Cristofolini, L., Dall'Ara, E., 2019b. Uncertainties of synchrotron microCT-based digital volume correlation bone strain measurements under simulated deformation. J. Biomech. 86, 232–237.
Croom, B.P., Burden, D., Jin, H., Vonk, N., Hoefnagels, J., Smaniotto, B., et al., 2021. Interlaboratory study of digital volume correlation error due to X-ray computed tomography equipment and scan parameters: an update from the DVC challenge. Exp. Mech. 61 (2), 395–410.
Dall'Ara, E., Peña-Fernández, M., Palanca, M., Giorgi, M., Cristofolini, L., Tozzi, G., 2017. Precision of digital volume correlation approaches for strain analysis in bone imaged with micro-computed tomography at different dimensional levels. Front. Mater. 4, 31.
Dall'Ara, E., Tozzi, G., 2022. Digital volume correlation for the characterization of musculoskeletal tissues: current challenges and future developments. Front. Bioeng. Biotechnol. 10 (2022), 1–13.
de Bournonville, S., Vangrunderbeeck, S., Ly, H.G.T., Geeroms, C., De Borggraeve, W.M., Parac-Vogt, T.N., et al., 2020. Exploring polyoxometalates as non-destructive staining agents for contrast-enhanced microfocus computed tomography of biological tissues. Acta Biomater. 105, 253–262. https://doi.org/10.1016/j.actbio.2020.01.038.
Dekoster, K., Decaesteker, T., Berghen, N., Van den Broucke, S., Jonckheere, A.C., Wouters, J., et al., 2020. Longitudinal micro-computed tomography-derived biomarkers quantify non-resolving lung fibrosis in a silicosis mouse model. Sci. Rep. 10 (1), 1. https://doi.org/10.1038/s41598-020-73056-6.
Deyhle, Jr RT., Krüger, R., Fardin, L., Mahmutovic Persson, I., Cercos-Pita, J.L., Perchiazzi, G., et al., 2025. Nanoscale structural alteration of lung collagen in response to strain and bleomycin injury. Sci. Rep. 15 (1), 21178.
Didziokas, M., Jones, D., Alazmani, A., Steacy, M., Pauws, E., Moazen, M., 2024. Multiscale mechanical characterisation of the craniofacial system under external forces. Biomech. Model. Mechanobiol. 23 (2), 675–685.
Eckermann, M., Frohn, J., Reichardt, M., Osterhoff, M., Sprung, M., Westermeier, F., et al., 2020. 3D virtual pathohistology of lung tissue from Covid-19 patients based on phase contrast X-ray tomography. eLife 9, e60408.
Garavelli, C., Aldieri, A., Palanca, M., Dall'Ara, E., Viceconti, M., 2025. Comparing the predictions of CT-based subject-specific finite element models of human metastatic vertebrae with digital volume correlation measurements. Biomech. Model. Mechanobiol. 24 (3), 1017–1030.
Gattinoni, L., Carlesso, E., Caironi, P., 2012. Stress and strain within the lung. Curr. Opin. Crit. Care 18 (1), 42–47.
Ginsberg, A.P., 2009. Inorganic Syntheses, vol. 27. John Wiley & Sons.
Goerner, F.L., Clarke, G.D., 2011. Measuring signal-to-noise ratio in partially parallel imaging MRI. Med. Phys. 38 (9), 5049–5057.
Herrmann, J., Tawhai, M.H., Kaczka, D.W., 2018. Parenchymal strain heterogeneity during oscillatory ventilation: why two frequencies are better than one. J. Appl. Physiol. 124 (3), 653–663.
Karagiannidis, E., Papazoglou, A.S., Sofidis, G., Chatzinikolaou, E., Keklikoglou, K., Panteris, E., et al., 2021. Micro-CT-based quantification of extracted thrombus burden characteristics and association with angiographic outcomes in patients with ST-elevation myocardial infarction: the QUEST-STEMI study. Frontiers in cardiovascular medicine 8, 646064.
Katsamenis, O.L., Olding, M., Warner, J.A., Chatelet, D.S., Jones, M.G., Sgalla, G., et al., 2019. X-ray micro-computed tomography for nondestructive three-dimensional (3D) X-ray histology. Am. J. Pathol. 189 (8), 1608–1620.
Langhe, E.D., Velde, G.V., Hostens, J., Himmelreich, U., Nemery, B., Luyten, F.P., et al., 2012. Quantification of lung fibrosis and emphysema in mice using Automated Micro-Computed tomography. PLoS One 7 (8), e43123. https://doi.org/10.1371/journal.pone.0043123.
Liu, L., Morgan, E.F., 2007a. Accuracy and precision of digital volume correlation in quantifying displacements and strains in trabecular bone. J. Biomech. 40 (15), 3516–3520.
Liu, L., Morgan, E.F., 2007b. Accuracy and precision of digital volume correlation in quantifying displacements and strains in trabecular bone. J. Biomech. 40 (15), 3516–3520.
Maes, A., Pestiaux, C., Marino, A., Balcaen, T., Leyssens, L., Vangrunderbeeck, S., et al., 2022. Cryogenic contrast-enhanced microCT enables nondestructive 3D quantitative histopathology of soft biological tissues. Nat. Commun. 13 (1), 1. https://doi.org/10.1038/s41467-022-34048-4.
Maghsoudi-Ganjeh, M., Sattari, S., Eskandari, M., 2021. Mechanical behavior of the airway wall in respiratory disease. Curr. Opin. Physiol. 22, 100445.
Mariano, C., Sattari, S., Quiros, K., Nelson, T., Eskandari, M., 2022. Examining lung mechanical strains as influenced by breathing volumes and rates using experimental digital image correlation. Respir. Res. 23 (1), 92.
Mariano, C.A., Sattari, S., Maghsoudi-Ganjeh, M., Tartibi, M., Lo, D.D., Eskandari, M., 2020. Novel mechanical strain characterization of ventilated ex vivo porcine and murine lung using digital image correlation. Front. Physiol. 11, 600492.
Mazy, L., Kerckhofs, G., 2025. A review of in-situ mechanical testing combined with X-ray microfocus computed tomography: application and current challenges for biological tissues. Tomography of Materials and Structures, 100062.
Nelson, T., Quiros, K., Dominguez, E., Ulu, A., Nordgren, T., Eskandari, M., 2023. Diseased and healthy murine local lung strains evaluated using digital image correlation. Sci. Rep. 13 (1), 4564.
Palanca, M., Bodey, A.J., Giorgi, M., Viceconti, M., Lacroix, D., Cristofolini, L., et al., 2017a. Local displacement and strain uncertainties in different bone types by digital volume correlation of synchrotron microtomograms. J. Biomech. 58, 27–36.
Palanca, M., Bodey, A.J., Giorgi, M., Viceconti, M., Lacroix, D., Cristofolini, L., et al., 2017b. Local displacement and strain uncertainties in different bone types by digital volume correlation of synchrotron microtomograms. J. Biomech. 58, 27–36.
Palanca, M., Tozzi, G., Cristofolini, L., 2016. The use of digital image correlation in the biomechanical area: a review. International Biomechanics 3 (1), 1–21. https://doi.org/10.1080/23335432.2015.1117395.
Pan, B., 2018. Digital image correlation for surface deformation measurement: historical developments, recent advances and future goals. Meas. Sci. Technol. 29 (8), 082001.
Pan, B., Wang, B., 2020. Some recent advances in digital volume correlation. Opt Laser. Eng. 135, 106189.
Paraskevoulakos, C., Ghosh, S., Andriollo, T., Michel, A., 2024. Sensitivity study using synthetic 3D image datasets to investigate the effect of noise artefacts on digital volume correlation. Exp. Mech. 64 (5), 595–624.
Paula, L.F., Wellman, T.J., Winkler, T., Spieth, P.M., Güldner, A., Venegas, J.G., et al., 2016. Regional tidal lung strain in mechanically ventilated normal lungs. J. Appl. Physiol. 121 (6), 1335–1347.
Pelli, D.G., Bex, P., 2013. Measuring contrast sensitivity. Vis. Res. 90, 10–14.
Pennati, F., Leo, L., Ferrini, E., Sverzellati, N., Bernardi, D., Stellari, F.F., et al., 2023. Micro-CT-derived ventilation biomarkers for the longitudinal assessment of pathology and response to therapy in a mouse model of lung fibrosis. Sci. Rep. 13 (1), 4462.
Pétré, M., Balcaen, T., Schneidewind, P., Mazy, L., Pyka, G., Fehervary, H., et al., 2024. Screening staining agents for contrast-enhanced microCT of vascular tissues: assessing the effect on microstructural and mechanical properties. Tomography of Materials and Structures 6, 100038.
Reiser, J., Albers, J., Svetlove, A., Mertiny, M., Kommoss, F.K., Schwab, C., et al., 2024. Integrative imaging of Lung Micro structure: amplifying classical histology by paraffin block μCT and same-slide scanning electron microscopy. bioRxiv 2024–06.
Roux, S., Hild, F., Viot, P., Bernard, D., 2008. Three-dimensional image correlation from X-ray computed tomography of solid foam. Compos. Appl. Sci. Manuf. 39 (8), 1253–1265.
Sattari, S., Mariano, C.A., Vittalbabu, S., Velazquez, J.V., Postma, J., Horst, C., et al., 2020. Introducing a custom-designed volume-pressure machine for novel measurements of whole lung organ viscoelasticity and direct comparisons between positive-and negative-pressure ventilation. Front. Bioeng. Biotechnol. 8, 578762.
Schaad, L., Hlushchuk, R., Barré, S., Gianni-Barrera, R., Haberthür, D., Banfi, A., et al., 2017. Correlative imaging of the murine hind limb vasculature and muscle tissue by MicroCT and light microscopy. Sci. Rep. 7 (1), 41842.
Soriano, J.B., Kendrick, P.J., Paulson, K.R., Gupta, V., Abrams, E.M., Adedoyin, R.A., et al., 2020. Prevalence and attributable health burden of chronic respiratory diseases, 1990–2017: a systematic analysis for the Global Burden of Disease Study 2017. Lancet Respir. Med. 8 (6), 585–596.
Starovoyt, A., Pyka, G., Putzeys, T., Balcaen, T., Wouters, J., Kerckhofs, G., et al., 2023. Human cochlear microstructures at risk of electrode insertion trauma, elucidated in 3D with contrast-enhanced microCT. Sci. Rep. 13 (1), 2191.
Steiner, L., Synek, A., Pahr, D.H., 2020. Comparison of different microCT-based morphology assessment tools using human trabecular bone. Bone reports 12, 100261.
Tielemans, B., Dekoster, K., Verleden, S.E., Sawall, S., Leszczyński, B., Laperre, K., et al., 2020. From mouse to man and back: closing the correlation gap between imaging and histopathology for lung diseases. Diagnostics 10 (9), 9. https://doi.org/10.3390/diagnostics10090636.
Tozzi, G., Zhang, Q.H., Tong, J., 2014. Microdamage assessment of bone-cement interfaces under monotonic and cyclic compression. J. Biomech. 47 (14), 3466–3474.

Vande, Velde G., De Langhe, E., Poelmans, J., Bruyndonckx, P., d'Agostino, E., Verbeken, E., et al., 2015. Longitudinal in vivo microcomputed tomography of mouse lungs: no evidence for radiotoxicity. Am. J. Physiol. Lung Cell. Mol. Physiol. 309 (3), L271–L279.

Vande, Velde G., Poelmans, J., De Langhe, E., Hillen, A., Vanoirbeek, J., Himmelreich, U., et al., 2016. Longitudinal micro-CT provides biomarkers of lung disease that can be used to assess the effect of therapy in preclinical mouse models, and reveal compensatory changes in lung volume. Dis. Model. Mech. 9 (1), 91–98.

Vasilescu, D.M., Knudsen, L., Ochs, M., Weibel, E.R., Hoffman, E.A., 2012. Optimized murine lung preparation for detailed structural evaluation via micro-computed tomography. J. Appl. Physiol. 112 (1), 159–166.

Wang, B., Pan, B., 2018. Incremental digital volume correlation method with nearest subvolume offset: an accurate and simple approach for large deformation measurement. Adv. Eng. Software 116, 80–88.

Zhu, M.L., Zhang, Q.H., Lupton, C., Tong, J., 2016. Spatial resolution and measurement uncertainty of strains in bone and bone–cement interface using digital volume correlation. J. Mech. Behav. Biomed. Mater. 57, 269–279.